THE JOURNAL OF PHYSICAL CHEMISTRY Letters

pubs.acs.org/JPCL Letter

Inter- and Intragrain Inhomogeneity in 2D Perovskite Thin Films Revealed by Relative Grain Orientation Imaging Using Low-Frequency Polarized Raman Microspectroscopy

Shogo Toda, Naoya Yanagita, Efat Jokar, Eric Wei-Guang Diau, and Shinsuke Shigeto*

Cite This: *J. Phys. Chem. Lett.* 2020, 11, 3871−3876 Read Online

ACCESS | Metrics & More | Article Recommendations | Supporting Information

ABSTRACT: Two-dimensional (2D) organic−inorganic hybrid lead halide perovskites make up an emerging class of semiconductor materials for optoelectronic applications such as solar cells. The grain structure of polycrystalline 2D perovskites is one of the key factors that dictate their functionality in the devices, but currently available methods for in situ, chemically specific characterization of 2D perovskite grains are scarce. Here we show that ultra-low-frequency polarized Raman microspectroscopy is a facile yet powerful tool for visualizing relative grain orientations within 2D perovskite thin films. We demonstrate this method on the simplest 2D perovskite, $(CH_3(CH_2)_3NH_3)_2PbI_4$. Hierarchical clustering and detailed band decomposition analysis of the low-frequency polarized Raman imaging data reveal not only relative grain orientations but also intragrain inhomogeneity. We envisage that with high chemical specificity, this method will find broad applications ranging from other 2D perovskites to perovskite-based optoelectronic devices.

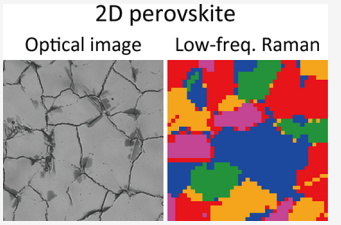

Organic−inorganic hybrid halide perovskites have been in the spotlight of materials research for the past decade because of their excellent properties that make them suitable for a variety of optoelectronic applications, including photovoltaics, light-emitting diodes, lasers, and photodetectors.[1,2] Among these applications, all-solid-state solar cells using methylammonium lead halides $MAPbX_3$ (MA = CH_3NH_3; X = Cl, Br, or I) and analogues as a light harvester are the most vigorously pursued, and their certified power conversion efficiency (PCE) has now exceeded 25%.[3] Besides being highly efficient, perovskite solar cells are easily solution-processable and cost-effective. However, their poor stability and poor versatility remain major challenges in the commercialization of perovskite solar cells. A new member of the family of hybrid perovskites, two-dimensional (2D) perovskites, has recently emerged as a promising candidate that can surmount these limitations.[4−6] 2D lead halide perovskites with the general formula $(A')_mA_{n-1}Pb_nX_{3n+1}$ (m = 1 for a divalent cation, and m = 2 for a monovalent cation) consist of alternating layers of the bulky organic cation A′ (e.g., long-chain alkyl ammonium) and inorganic $A_{n-1}Pb_nX_{3n+1}$ slabs. The 2D perovskites are better than their three-dimensional (3D) counterparts in terms of long-term stability to moisture owing to the hydrophobic nature of the spacer cation layer and in terms of chemical versatility because of their high compositional/structural diversity.[6]

A crucial key for further exploiting 2D perovskites for next-generation optoelectronics is to elucidate the polycrystalline microstructure characteristic of perovskite thin films. Perovskite thin films are polycrystalline in nature and comprise a large number of nano- to micrometer-sized grains and grain boundaries (GBs) between them. Crystal defects at GBs often lead to the formation of localized energy states within the band gap, which may trap photogenerated charge carriers and act as nonradiative recombination sites.[7] For highly efficient perovskite solar cells, it is therefore important to reduce GBs by, for example, enlarging the grain size and controlling the grain orientation.[8,9] On the other hand, many studies of both 2D and 3D perovskites have shown that GBs substantially enhance charge carrier transport.[10−13] In general, the properties of GBs are affected by the orientation of the surrounding grains. In the case of 2D perovskites, a competition results between horizontal and vertical orientations in which the inorganic 2D sheets align parallel and perpendicular to the substrate, respectively,[14−16] so that knowing the grain orientation is particularly important. Nevertheless, methods that can visualize grain orientation within 2D perovskite films are scant. Scanning electron microscopy (SEM) and atomic force microscopy (AFM) are arguably among the most commonly used, but these methods can detect only surfaces and inherently lack chemical specificity.

Herein, we report on the use of low-frequency polarized Raman (LFPR) microspectroscopy to visualize relative grain orientations within thin films of the simplest member of the family of 2D perovskites, BA_2PbI_4 [BA = $CH_3(CH_2)_3NH_3$; see

Received: March 29, 2020
Accepted: April 27, 2020
Published: April 27, 2020

https://dx.doi.org/10.1021/acs.jpclett.0c00992
J. Phys. Chem. Lett. 2020, 11, 3871−3876

Figure 1a for a schematic of the crystal structure]. Using a laboratory-built confocal Raman microspectrometer (see ref 17

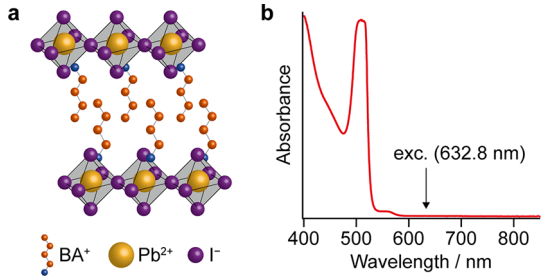

Figure 1. (a) Schematic of the crystal structure of BA_2PbI_4. (b) Absorption spectrum of the BA_2PbI_4 film used in this work.

and the Supporting Information for details of the apparatus), we are able to measure, under various polarization configurations, space-resolved Raman spectra of BA_2PbI_4 thin films in the extremely low-frequency region down to as low as ~10 cm^{-1}, which are sensitive to crystal lattice vibrations (phonon modes).[18,19] The Raman intensity of a lattice mode is proportional to $\left|\sum_{\rho,\sigma}(\rho\cdot\mathbf{e}_s)(\sigma\cdot\mathbf{e}_i)a_{\rho\sigma}\right|^2$, where $a_{\rho\sigma}$ (crystal-fixed coordinates $\rho, \sigma = x, y, z$) is the $\rho\sigma$ element of the Raman scattering tensor $\mathbf{a}$ and $\mathbf{e}_i$ and $\mathbf{e}_s$ are the polarization vectors of the incident and scattered light, respectively. Therefore, LFPR spectra measured with different combinations of $\mathbf{e}_i$ and $\mathbf{e}_s$ can provide information about crystal orientation if the symmetry of the mode is known. Hierarchical cluster analysis (HCA) and thorough band decomposition analysis of the LFPR imaging results allow for grain orientation imaging of the 2D perovskite film and reveal distinct inter- and intragrain orientational inhomogeneity.

BA_2PbI_4 ($m = 2$; $n = 1$), exhibiting the intuitive horizontal growth of the film different from that of $BA_2MA_{n-1}Pb_nI_{3n+1}$ with $n \geq 3$,[14,15] provides an interesting starting point for the study of grain orientation in 2D perovskites. Figure 1b shows the absorption spectrum of a BA_2PbI_4 thin film spin-coated on a glass coverslip (see the Supporting Information for sample preparation). Our Raman excitation wavelength of 632.8 nm is well above the absorption band edge at ~534 nm, ensuring that the BA_2PbI_4 sample does not absorb the excitation laser light. This off-resonant excitation is essential for obtaining true perovskite Raman spectra because perovskites tend to decompose when irradiated with laser light they absorb.[20,21]

First, we performed Raman imaging experiments on a small area (20 μm × 20 μm; see the optical micrograph in Figure 2a) of a BA_2PbI_4 thin film to obtain a rough idea of the spectral features associated with the grains and GBs therein. As one can see from Figure 2a, the prepared BA_2PbI_4 film shows platelike grains tens of micrometers in size (see Figure S1 for a SEM image of a BA_2PbI_4 film). The space-resolved Raman spectra recorded at three distinct points A–C (indicated in Figure 2a) within the 2D perovskite film are shown in Figure 2b for both low- and high-frequency regions. The low-frequency spectra provide structural fingerprints through lattice Raman bands, whereas the high-frequency spectra provide chemical fingerprints via intramolecular bands. All sharp Raman bands observed in the high-frequency region arise from vibrational modes of the organic cation. By reference to the mode assignments of $MAPbI_3$,[22] the bands at 1474 and 1578 cm^{-1} can be assigned to the symmetric and asymmetric NH_3^+

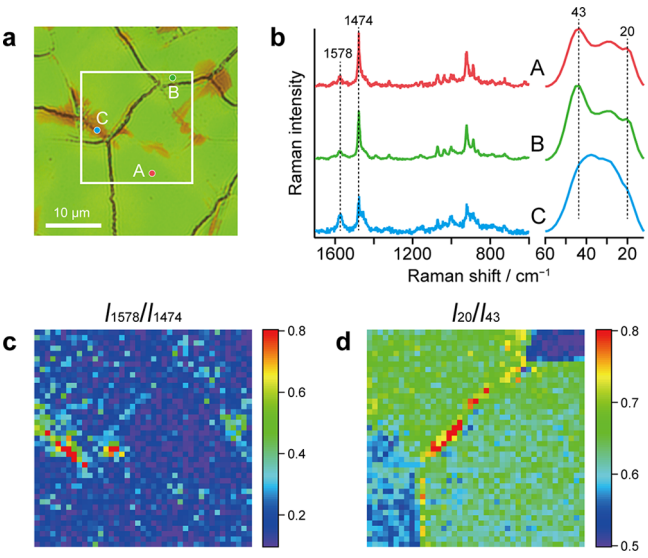

Figure 2. (a) Optical micrograph of a 2D perovskite BA_2PbI_4 thin film formed on a glass coverslip. The area in which we performed the Raman imaging measurement is indicated by a white square. Note that this micrograph does not represent the actual color of the sample due to the dichroic mirror used in the apparatus; the film actually looked orange. Scale bar of 10 μm. (b) High-frequency (600–1700 cm^{-1}) and low-frequency (10–60 cm^{-1}) Raman spectra measured at points A–C indicated in panel a. The former has been vertically enlarged by a factor of 50 to facilitate comparison with the latter. (c and d) Images of the Raman intensity ratios I_{1578}/I_{1474} and I_{20}/I_{43}, respectively, in rainbow pseudocolor. The image size is 20 μm × 20 μm in both images.

bending modes, respectively. The high-frequency Raman spectra at points A (Figure 2b, red) and B (Figure 2b, green), which were chosen from inside different grains, are almost identical in pattern to each other. In contrast, the corresponding low-frequency spectra do exhibit a noticeable difference in the relative peak intensity at 20 and 43 cm^{-1}; namely, the intensity ratio of the peak at 20 cm^{-1} to that at 43 cm^{-1}, I_{20}/I_{43}, is smaller at point B than at point A. The Raman spectrum at point C on a grain boundary (Figure 2b, cyan) shows deteriorated signal intensities in the high-frequency region and a featureless broad pattern in the low-frequency region. Considering that some change in color, which looks brown in Figure 2a, is identified at point C, this result suggests that the perovskite was locally degraded probably by the atmospheric moisture.

To examine whether these differences found at the specific points are general, we plot the images of the Raman intensity (peak intensity) ratios I_{1578}/I_{1474} (Figure 2c) and I_{20}/I_{43} (Figure 2d). Although the thickness of the perovskite film might vary from point to point, these ratio images compensate for such morphological variations. Consistent with the representative spectra shown in Figure 2b, the intensity ratio I_{1578}/I_{1474} (Figure 2c) displays a nearly uniform distribution within the scanned area except for several regions, including point C, which agree fairly well with the brown parts in the optical micrograph (Figure 2a). The intensity ratio I_{20}/I_{43} (Figure 2d) is similar across the grain containing point A but is significantly weaker in the adjacent grain containing point B. It also delineates the boundary between two grains (see the red region in Figure 2d). From the comparison of the two images, we confirm that while the high-frequency Raman spectrum is

https://dx.doi.org/10.1021/acs.jpclett.0c00992
J. Phys. Chem. Lett. 2020, 11, 3871–3876

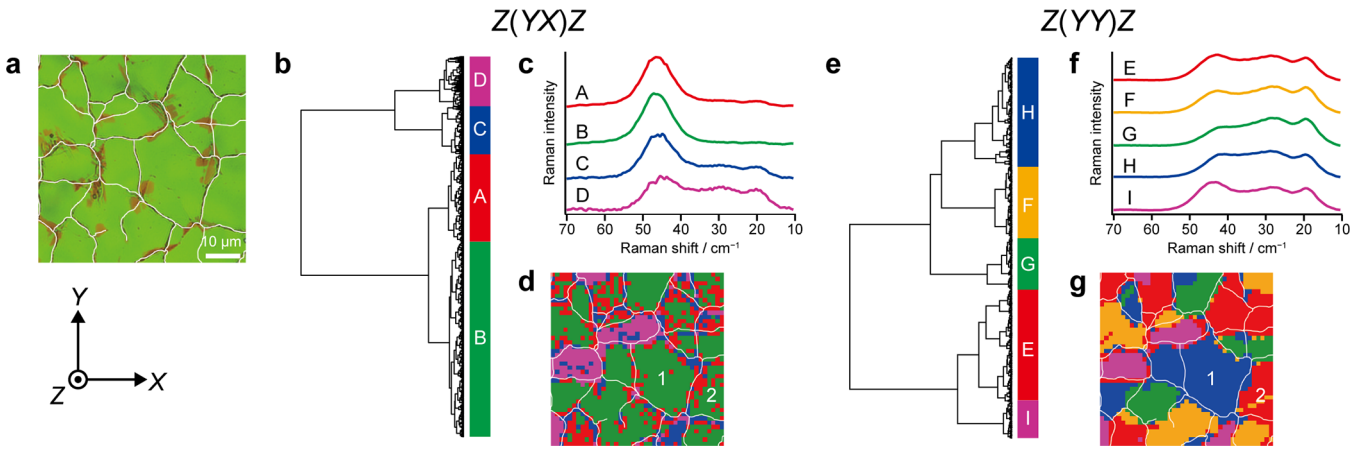

Figure 3. (a) Optical micrograph of the scanned area in a 2D perovskite BA_2PbI_4 thin film formed on a glass coverslip (different from that in Figure 2a). The GBs that have been extracted from this image are depicted with white lines as a guide to the eye. Scale bar of 10 μm. (b–d) HCA results for the $Z(YX)Z$ LFPR imaging data of the BA_2PbI_4 film. (b) Dendrogram showing a classification of the data into four clusters A–D. (c) Mean Raman spectra and (d) spatial distributions of clusters A–D. (e–g) HCA results for the $Z(YY)Z$ LFPR imaging data of the BA_2PbI_4 film. (e) Dendrogram showing a classification of the data into five clusters E–I. (f) Mean Raman spectra and (g) spatial distributions of clusters E–I.

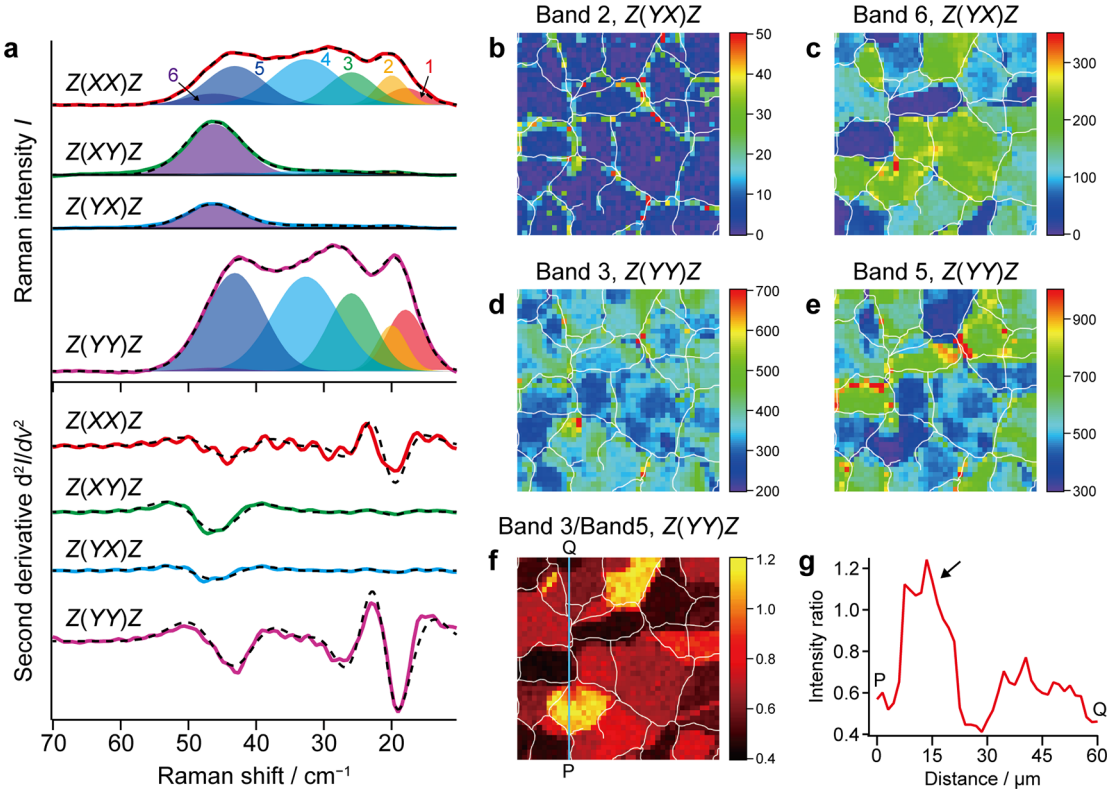

Figure 4. (a) Averaged LFPR spectra (top panel, solid lines) and their second derivatives (bottom panel, solid lines) for polarization configurations $Z(XX)Z$, $Z(XY)Z$, $Z(YX)Z$, and $Z(YY)Z$. The best fits obtained using six Gaussian bands 1–6 are shown as dashed lines. (b–e) Raman images of band 2 for $Z(YX)Z$, band 6 for $Z(YX)Z$, band 3 for $Z(YY)Z$, and band 5 for $Z(YY)Z$, respectively, in rainbow pseudocolor. (f) Image of the intensity ratio of band 3 to band 5 for $Z(YY)Z$, in pseudocolor with yellow representing the highest intensity ratio, red moderate, and black the lowest. (g) Line profile along the cyan line PQ shown in panel f, exhibiting a significant increase in the intensity ratio inside a grain (marked by the arrow).

basically silent to the inhomogeneous polycrystalline structure, the low-frequency lattice Raman spectrum can clearly differentiate between different grains.

With the success of demonstrating the ability of low-frequency Raman spectra to make a sharp distinction between 2D perovskite grains, we carried out similar Raman imaging experiments on a larger area containing many more grains (60 μm × 60 μm; see the optical micrograph in Figure 3a) of another fresh BA_2PbI_4 film under four different polarization configurations: $Z(XX)Z$, $Z(XY)Z$, $Z(YX)Z$, and $Z(YY)Z$ (see Figure 3a for the definition of the space-fixed coordinates). Here we adopt the Porto notation[23] $\mathbf{k}_i(\mathbf{e}_i\mathbf{e}_s)\mathbf{k}_s$, where $\mathbf{k}_i$ and $\mathbf{k}_s$ denote the wave vectors of the incident and scattered light, respectively. Because a total of four sets of LFPR imaging

https://dx.doi.org/10.1021/acs.jpclett.0c00992
J. Phys. Chem. Lett. 2020, 11, 3871–3876

experiments required approximately 2 h, care had to be taken to ensure that the perovskite did not degrade during the experiments. To this end, we captured optical micrographs before and after the experiments, which evidenced a change in neither the color nor the morphology of the film (Figure S2). In addition, we did not find any appreciable decrease in overall Raman intensity.

To classify the grains on the basis of the low-frequency spectral pattern, we analyzed the obtained LFPR imaging data with HCA (see the Supporting Information for details of the analysis). The results are shown in Figure 3b−d for $Z(YX)Z$ and Figure 3e−g for $Z(YY)Z$, and those for $Z(XX)Z$ and $Z(XY)Z$ are given in Figure S3. The dendrogram (Figure 3b) shows that the LFPR spectra measured under the $Z(YX)Z$ configuration can be classified into four clusters that are highly similar (denoted A−D). The mean Raman spectra and spatial distributions (cluster maps) of the four clusters are shown in panels c and d of Figure 3, respectively. It is evident from Figure 3d that there are two types of grains in the scanned area corresponding to clusters B (green) and D (purple). Clusters A (red) and C (blue) are localized on and around GBs. Likewise, the $Z(YY)Z$ LFPR spectra can be grouped into five clusters (denoted E−I), as shown in Figure 3e. The mean spectra of the five clusters (Figure 3f) differ considerably from those obtained for $Z(YX)Z$ (Figure 3c), indicating a large polarization dependence of the low-frequency spectral pattern of the 2D perovskite. Compared to the $Z(YX)Z$ configuration, the $Z(YY)Z$ configuration manifests a more detailed grain structure. To see this, compare, for example, grains 1 and 2 indicated in panels d and g of Figure 3. These grains belong to the same cluster B (green) in $Z(YX)Z$ but fall into different clusters E (red) and H (blue) in $Z(YY)Z$. A high degree of inhomogeneity in the BA_2PbI_4 film has thus been visualized.

Although the cluster maps (Figure 3d,g) have enabled differentiation of perovskite grains, the classification is simply based on spectral similarities. The resulting mean cluster spectra (Figure 3c,f) cannot be directly associated with the grain properties that make the differentiation possible. By the same token, they cannot visualize intragrain inhomogeneity either. The marked polarization-dependent variation in the low-frequency spectral pattern is a consequence of lattice vibrational modes of different symmetry and its relationship with grain orientation with respect to the polarization of the incident light. To clarify this relationship, decomposition of the LFPR spectra into individual lattice modes is necessary.

To cope with the difficulty in accurately decomposing the broad LFPR spectra, we took their second derivatives into account. The averaged Raman spectra and their second derivatives for the four polarization configurations are shown as solid lines in the top and bottom panels of Figure 4a, respectively. First, we deduced the number of underlying bands from the negative peaks seen in the second-derivative spectra, which was found to be six. Next, we fitted the four LFPR spectra and their second derivatives simultaneously using six Gaussian functions (denoted 1−6 in order of ascending frequency) and their second derivatives. The best fits are shown as dashed lines in Figure 4a, and the peak position and bandwidth so determined of each Gaussian band are listed in Table S1. The decomposition into six bands is in qualitative agreement with well-resolved low-frequency Raman spectra of 2D perovskites $(C_xH_{2x+1}NH_3)_2PbI_4$ (x = 4−9) at 77 K reported recently by Mauck et al.[24] Five of the obtained six Gaussian bands [bands 1−5 for $Z(XX)Z$ and $Z(YY)Z$; bands 2−6 for $Z(XY)Z$ and $Z(YX)Z$] were then used to fit the Raman spectrum at each point in the scanned area for each polarization configuration. Representative fitted results shown in Figure S4 are satisfactory, verifying our fitting analysis with five components.

On the basis of the spectral features discussed above, we here focus our attention on pairs of Raman bands (2,6) and (3,5) in $Z(YX)Z$ and $Z(YY)Z$, the area intensity images of which are displayed in Figure 4b−e. Band 2 (peaking at 20 cm^{-1}) is observed exclusively at GBs, as expected from Figure 2d. This enhanced intensity of band 2 at GBs is likely due to an altered Raman scattering tensor of the corresponding phonon mode of defect structures. Band 6 (peaking at 46 cm^{-1}) is the dominating band in the $Z(XY)Z$ and $Z(YX)Z$ configurations (see Figure 4a, top panel), and its Raman image appears to mirror the cluster map in Figure 3d. A highly inhomogeneous distribution of the relative grain orientation is not clearly seen in the intensity images of bands 3 and 5 for $Z(YY)Z$ per se but is evident in the ratio image of these bands (Figure 4f). The ratio image well resembles the cluster map for $Z(YY)Z$ (Figure 3g), with the yellow region corresponding to cluster G (green), the red region to clusters F (yellow) and H (blue), and the black region to clusters E (red) and I (purple). Importantly, we also find intragrain inhomogeneity in the ratio image. The line profile depicted in Figure 4g suggests a variation of the intensity ratio inside a yellow-colored grain that is significantly greater than the noise level (marked by the arrow).

In conclusion, we have presented relative grain orientation imaging of 2D perovskite BA_2PbI_4 thin films by means of LFPR microspectroscopy. Unlike SEM and AFM, this method can be applied to in situ measurements of optoelectronic devices such as solar cells in which the perovskite layer is sandwiched between other materials (e.g., electron and hole transport layers). Furthermore, the high chemical specificity imparted to Raman spectroscopy should make the present method particularly useful in visualizing perovskites composed of mixed cations.[25−27] The high-frequency region measured simultaneously with the low-frequency region as in Figure 2b facilitates differentiation between the different cations and hence their grains. By moving the excitation wavelength to longer wavelengths, this method becomes applicable to other 2D perovskites that usually exhibit a band gap smaller than that of BA_2PbI_4. Accurate measurements on perovskite single crystals whose orientations are known with respect to the space-fixed coordinates will provide us with quantitative information about the Raman scattering tensor elements of the lattice modes, thus enabling "absolute" grain orientation imaging.[28]

■ ASSOCIATED CONTENT

Supporting Information

The Supporting Information is available free of charge at https://pubs.acs.org/doi/10.1021/acs.jpclett.0c00992.

Experimental section, list of fitting parameters, reference SEM image, optical micrographs of the sample, HCA results for the $Z(XX)Z$ and $Z(XY)Z$ configurations, and representative results of the band decomposition analysis (PDF)

https://dx.doi.org/10.1021/acs.jpclett.0c00992
J. Phys. Chem. Lett. 2020, 11, 3871−3876

AUTHOR INFORMATION

Corresponding Author

Shinsuke Shigeto − *Department of Chemistry, Graduate School of Science and Technology, Kwansei Gakuin University, Hyogo 669-1337, Japan;* orcid.org/0000-0002-2035-2068; Email: shigeto@kwansei.ac.jp

Authors

Shogo Toda − *Department of Chemistry, Graduate School of Science and Technology, Kwansei Gakuin University, Hyogo 669-1337, Japan*

Naoya Yanagita − *Department of Chemistry, Graduate School of Science and Technology, Kwansei Gakuin University, Hyogo 669-1337, Japan*

Efat Jokar − *Department of Applied Chemistry and Institute of Molecular Science and Center for Emergent Functional Matter Science, National Chiao Tung University, Hsinchu 30010, Taiwan*

Eric Wei-Guang Diau − *Department of Applied Chemistry and Institute of Molecular Science and Center for Emergent Functional Matter Science, National Chiao Tung University, Hsinchu 30010, Taiwan;* orcid.org/0000-0001-6113-5679

Complete contact information is available at: https://pubs.acs.org/10.1021/acs.jpclett.0c00992

Notes

The authors declare no competing financial interest.

ACKNOWLEDGMENTS

This work was supported by JSPS KAKENHI Grants JP19H02821 (S.S.) and JP18J20312 (S.T.), the Ministry of Science and Technology, Taiwan [Grant MOST108-2119-M-009-004 (E.W.-G.D.)], and the Center for Emergent Functional Matter Science of National Chiao Tung University from The Featured Areas Research Center Program within the framework of the Higher Education SPROUT Project by the Ministry of Education (MOE) in Taiwan (E.W.-G.D. and E.J.). S.S. is grateful for partial support from the Kawanishi Memorial ShinMaywa Education Foundation.

REFERENCES

(1) Stranks, S. D.; Snaith, H. J. Metal-Halide Perovskites for Photovoltaic and Light-Emitting Devices. *Nat. Nanotechnol.* **2015**, *10*, 391−402.

(2) Sutherland, B. R.; Sargent, E. H. Perovskite Photonic Sources. *Nat. Photonics* **2016**, *10*, 295−302.

(3) NREL. Best Research-Cell Efficiency Chart. https://www.nrel.gov/pv/cell-efficiency.html (accessed 2020-03-26).

(4) Saidaminov, M. I.; Mohammed, O. F.; Bakr, O. M. Low-Dimensional-Networked Metal Halide Perovskites: The Next Big Thing. *ACS Energy Lett.* **2017**, *2*, 889−896.

(5) Ortiz-Cervantes, C.; Carmona-Monroy, P.; Solis-Ibarra, D. Two-Dimensional Halide Perovskites in Solar Cells: 2D or Not 2D? *ChemSusChem* **2019**, *12*, 1560−1575.

(6) Mao, L.; Stoumpos, C. C.; Kanatzidis, M. G. Two-Dimensional Hybrid Halide Perovskites: Principles and Promises. *J. Am. Chem. Soc.* **2019**, *141*, 1171−1190.

(7) Ono, L. K.; Liu, S.; Qi, Y. Reducing Detrimental Defects for High-Performance Metal Halide Perovskite Solar Cells. *Angew. Chem., Int. Ed.* **2020**, *59*, 6676−6698.

(8) Lian, X.; Chen, J.; Qin, M.; Zhang, Y.; Tian, S.; Lu, X.; Wu, G.; Chen, H. The Second Spacer Cation Assisted Growth of a 2D Perovskite Film with Oriented Large Grain for Highly Efficient and Stable Solar Cells. *Angew. Chem., Int. Ed.* **2019**, *58*, 9409−9413.

(9) Fei, C.; Zhou, M.; Ogle, J.; Smilgies, D.-M.; Whittaker-Brooks, L.; Wang, H. Self-Assembled Propylammonium Cations at Grain Boundaries and the Film Surface to Improve the Efficiency and Stability of Perovskite Solar Cells. *J. Mater. Chem. A* **2019**, *7*, 23739−23746.

(10) Li, J.-J.; Ma, J.-Y.; Ge, Q.-Q.; Hu, J.-S.; Wang, D.; Wan, L.-J. Microscopic Investigation of Grain Boundaries in Organolead Halide Perovskite Solar Cells. *ACS Appl. Mater. Interfaces* **2015**, *7*, 28518−28523.

(11) Shao, Y.; et al. Grain Boundary Dominated Ion Migration in Polycrystalline Organic-Inorganic Halide Perovskite Films. *Energy Environ. Sci.* **2016**, *9*, 1752−1759.

(12) Yuan, M.; et al. Perovskite Energy Funnels for Efficient Light-Emitting Diodes. *Nat. Nanotechnol.* **2016**, *11*, 872−877.

(13) Wang, K.; Wu, C.; Jiang, Y.; Yang, D.; Wang, K.; Priya, S. Distinct Conducting Layer Edge States in Two-Dimensional (2D) Halide Perovskite. *Sci. Adv.* **2019**, *5*, No. eaau3241.

(14) Cao, D. H.; Stoumpos, C. C.; Farha, O. K.; Hupp, J. T.; Kanatzidis, M. G. 2D Homologous Perovskites as Light-Absorbing Materials for Solar Cell Applications. *J. Am. Chem. Soc.* **2015**, *137*, 7843−7850.

(15) Chen, A. Z.; Shiu, M.; Ma, J. H.; Alpert, M. R.; Zhang, D.; Foley, B. J.; Smilgies, D.-M.; Lee, S.-H.; Choi, J. J. Origin of Vertical Orientation in Two-Dimensional Metal Halide Perovskites and Its Effect on Photovoltaic Performance. *Nat. Commun.* **2018**, *9*, 1336.

(16) Quintero-Bermudez, R.; Gold-Parker, A.; Proppe, A. H.; Munir, R.; Yang, Z.; Kelley, S. O.; Amassian, A.; Toney, M. F.; Sargent, E. H. Compositional and Orientational Control in Metal Halide Perovskites of Reduced Dimensionality. *Nat. Mater.* **2018**, *17*, 900−907.

(17) Matsuda, A.; Sakaguchi, N.; Shigeto, S. Can Cells Maintain Their Bioactivity in Ionic Liquids? A Novel Single-Cell Assessment by Raman Microspectroscopy. *J. Raman Spectrosc.* **2019**, *50*, 768−777.

(18) Chang, C.-F.; Wang, S.-C.; Shigeto, S. In Situ Ultralow-Frequency Raman Tracking of the Polymorphic Transformation of Crystalline 1,1′-Binaphthyl. *J. Phys. Chem. C* **2014**, *118*, 2702−2709.

(19) Chang, C.-F.; Okajima, H.; Hamaguchi, H.; Shigeto, S. Imaging Molecular Crystal Polymorphs and Their Polycrystalline Microstructures in Situ by Ultralow-Frequency Raman Spectroscopy. *Chem. Commun.* **2014**, *50*, 12973−12976.

(20) Zhou, Y.; Garces, H. F.; Padture, N. P. Challenges in the Ambient Raman Spectroscopy Characterization of Methylammonium Lead Triiodide Perovskite Thin Films. *Front. Optoelectron.* **2016**, *9*, 81−86.

(21) Pistor, P.; Ruiz, A.; Cabot, A.; Izquierdo-Roca, V. Advanced Raman Spectroscopy of Methylammonium Lead Iodide: Development of a Non-Destructive Characterisation Methodology. *Sci. Rep.* **2016**, *6*, 35973.

(22) Glaser, T.; et al. Infrared Spectroscopic Study of Vibrational Modes in Methylammonium Lead Halide Perovskites. *J. Phys. Chem. Lett.* **2015**, *6*, 2913−2918.

(23) Damen, T. C.; Porto, S. P. S.; Tell, B. Raman Effect in Zinc Oxide. *Phys. Rev.* **1966**, *142*, 570−574.

(24) Mauck, C. M.; France-Lanord, A.; Hernandez Oendra, A. C.; Dahod, N. S.; Grossman, J. C.; Tisdale, W. A. Inorganic Cage Motion Dominates Excited-State Dynamics in 2D-Layered Perovskites $(C_xH_{2x+1}NH_3)_2PbI_4$ (x = 4−9). *J. Phys. Chem. C* **2019**, *123*, 27904−27916.

(25) McMeekin, D. P.; et al. A Mixed-Cation Lead Mixed-Halide Perovskite Absorber for Tandem Solar Cells. *Science* **2016**, *351*, 151−155.

(26) Xu, F.; Zhang, T.; Li, G.; Zhao, Y. Mixed Cation Hybrid Lead Halide Perovskites with Enhanced Performance and Stability. *J. Mater. Chem. A* **2017**, *5*, 11450−11461.

(27) Gao, P.; Bin Mohd Yusoff, A. R.; Nazeeruddin, M. K. Dimensionality Engineering of Hybrid Halide Perovskite Light Absorbers. *Nat. Commun.* **2018**, *9*, 5028.

(28) Ilchenko, O.; Pilgun, Y.; Kutsyk, A.; Bachmann, F.; Slipets, R.; Todeschini, M.; Okeyo, P. O.; Poulsen, H. F.; Boisen, A. Fast and

Quantitative 2D and 3D Orientation Mapping Using Raman Microscopy. *Nat. Commun.* **2019**, *10*, 5555.

https://dx.doi.org/10.1021/acs.jpclett.0c00992
J. Phys. Chem. Lett. 2020, 11, 3871−3876